PAPER

Unveiling the enhanced photoelectrochemical and photocatalytic properties of reduced graphene oxide for photodegradation of methylene blue dye†

Valerie Ling Er Siong, [ID] Xin Hong Tai, [ID] Kian Mun Lee, Joon Ching Juan [ID] and Chin Wei Lai [ID]*

Graphene oxide (GO) and reduced graphene oxide (rGO) can act as metal-free photocatalysts to remove aqueous dye pollutants under light illumination. However, there is some disparity in past reports on the origin of the photoactivity of GO and rGO for photodegradation of dye pollutants. In this work, the photoactivity of GO and rGO for methylene blue (MB) dye photodegradation were investigated with photoelectrochemical (PEC) measurements. The optimized rGO sample (G-2) exhibited a stable photocatalytic rate, which was 2.5 times higher than that of pure GO. PEC measurements revealed that the photocatalytic activity of G-2 was elevated due to higher photocurrent density, higher charge carrier density, and better charge separation. The changes in band gap and band positions of rGO were determined through optical characterization and Mott–Schottky (M–S) plots. Finally, the photocatalytic degradation mechanism of GO and rGO on MB dye was determined.

1. Introduction

Effluent wastewaters consisting of dye pollutants from the printing industry raise much concern due to their negative effects on the environment and ecological systems.[1,2] To remediate the water dye pollutant issue, several techniques such as adsorption, flocculation, ultrafiltration, *etc.* have been employed in the past.[3] Among these techniques, photocatalytic degradation is a clean and cost-effective method for water purification. In a typical photocatalytic degradation process, dye molecules are photodegraded into harmless compounds *via* photogenerated holes (h^+), superoxide radicals ($^{\bullet}O_2^-$), and hydroxyl radicals ($^{\bullet}OH$) on the surface of a photocatalyst.[4]

Carbon-based materials are frequently studied as a supporting component in various photocatalytic applications.[5–8] Among the carbon-based materials, graphene oxide (GO) and reduced graphene oxide (rGO) have shown promising results as stand-alone photocatalysts in photocatalytic dye degradation. For example, the photodegradation of resazurin, reactive black 5, congo red, methyl orange, rhodamine B, and methylene blue (MB) by GO, rGO, and heteroatom-doped GO.[9–21] In addition, our earlier work had shown that rGO synthesized *via* facile solvothermal method can completely photodegrade MB dye under UV illumination after process optimizations.[22] However,

there are some contradicting past reports on the origin of photoactivity of GO and rGO for dye photodegradation. For instance, Guardia *et al.* stated that GO under UV illumination degraded RhB *via* photoinduced heating of localized GO sheets and not photocatalytic degradation.[23] Moreover, there were studies which claimed that GO materials were not photoactive enough to photodegrade MO and orange II dyes.[24,25] The disparity in the literature suggests that a more detailed study on the dye photodegradation mechanism of GO and rGO as photocatalysts is needed.

To confirm and measure the ability of a photocatalyst to carry out photocatalytic degradation of dye, a series of photoelectrochemical (PEC) measurements were often deployed.[26–29] Nevertheless, to the best of our knowledge, the PEC measurement techniques have not been used to examine the photocatalytic degradation ability of GO/rGO photocatalysts for dye photodegradation yet. In this study, rGO was synthesized *via* autoclave solvothermal reduction from GO to photodegrade MB dye under UV light illumination. The physicochemical and PEC properties of the synthesized samples were conducted to unveil the origin of their photoactivity on dye photodegradation.

2. Experimental section

2.1. Materials

Synthetic graphite powder (<20.0 μm) was purchased from Sigma-Aldrich. Potassium peroxodisulphate (≥99%), diphosphorus pentoxide (≥99%), and ethanol (≥99.9%) were obtained from Merck & Co. $H_2SO_4 \geq 95–97\%$, $KMnO_4 \geq 99\%$,

Nanotechnology & Catalysis Research Centre (NANOCAT), Institute for Advanced Studies (IAS), University of Malaya, Kuala Lumpur, Malaysia. E-mail: cwlai@um.edu.my

$H_2O_2 \geq 30\%$, $HCl \geq 37\%$, and methylene blue (MB, C.I. 52015, $\geq 99\%$) were acquired from Friendemann Schmidt.

2.2. Preparation of rGO

GO was produced according to our previous work.[22] Then, 200 mg of synthesized GO powder was suspended in a solvent of 2 : 1 (volume) ethanol/deionized water mixture. The suspension was sonicated in ultrasonic bath for 30 min to produce a stable dispersion. Subsequently, the stable GO suspension was poured into autoclave and heated in oven (160 °C) for a certain duration. The autoclaved mixture was then subjected to vacuum filtration, and the resulting rGO was rinsed with deionized water. Finally, the rGO was dried in oven at 60 °C and grinded into powder. The as prepared rGO samples are indicated as G-X, where X representing the autoclave duration of 0, 1, 2, 4, and 8 h respectively.

2.3. Methods of characterization

Field emissions scanning electron microscope (FEI Quanta FEG 650) with attached energy dispersive X-ray spectrometer (EDX) was used to find out the morphology and elemental composition of selected samples. Raman spectroscopy was conducted with a Renishaw inVia Raman Microscope (514 nm Ar-ion laser, $500–3200$ cm^{-1}) to measure the degree of rGO reduction. Photoluminescence (PL) analysis was performed on selected samples using a Renishaw inVia Raman (325 nm Ar-ion laser, 400–900 nm). The crystalline phases of the samples were analysed by a PANalytical X-ray Diffractometer (XRD) (Cu Kα, $\lambda = 0.154$ nm) under 40 kV and 30 mA. The specific surface area (SSA), pore size, and pore volume were analysed in N_2 atmosphere at 77 K by a Micromeritics ASAP 2020 Surface Area and Porosity Analyzer. The light absorbance (200–600 nm) of the samples were measured by a Perkin Elmer Lambda 35 UV-Vis spectrophotometer. X-ray photoelectron spectroscopy (XPS) was scanned via a JEOL JPS9030 with MgKα X-ray source to investigate the chemical bonding of the samples.

2.4. Adsorption and photocatalytic activity measurements

20 mg of G-X sample was dispersed in 100 ml of 50 ppm MB solution. Dark adsorption was carried out to determine the adsorption and desorption equilibrium point. After reaching the adsorption–desorption equilibrium point, the MB solution was irradiated with 95 W UV-C light (light intensity of 2.4 mW cm^{-2} measured by Newport power meter 843-R) in a custom-made photoreactor[22] for 6 h. The light spectrum of the UV-C light is shown in Fig. S1.† At certain intervals, aliquots were analysed with UV-Vis for peak intensity at 664 nm. The adsorption removal% (% R_{ads}) and the photodegradation removal% (% R_{pho}) were calculated according to the following equations:

$$\% \ R_{ads} = \frac{C_{initial} - C_0}{C_{initial}} \times 100\% \tag{1}$$

$$\% \ R_{pho} = \frac{C_0 - C_t}{C_0} \times 100\%, \quad 0 \leq t \leq 6 \tag{2}$$

where $C_{initial}$, C_0, and C_t are the MB dye concentrations (ppm) at initial introduction, at adsorption and desorption equilibrium, and at time (t). Then, pseudo-first order kinetic equation was used to fit the photocatalytic degradation data as below:

$$-\ln\left(\frac{C_t}{C_0}\right) = kt \tag{3}$$

The symbol k (h^{-1}) is the pseudo-first order rate constant. The best G-X sample was tested for five photodegradation cycles with the same reaction conditions to determine the stability and reusability of the photocatalyst.

2.5. Photoelectrochemical measurements

Photoelectrochemical measurements of the selected samples were conducted with a Metrohm Autolab (PGSTAT302N) electrochemical workstation. A three-electrode cell setup was used, where the reference electrode was Ag/AgCl, counter electrode was Pt, and working electrode was fluorine-doped tin oxide (FTO) glass slides. Photocatalyst samples (1 cm^2) were deposited on the FTO glass via a doctor-blade coating method, where adhesive tape and glass rod were used as the spacer and frame. The electrolyte used for all analyses was aqueous 0.5 M Na_2SO_4 at pH 6.5. The light source for photocurrent was supplied by a 150 W xenon lamp with 0.2 V bias. Electrochemical impedance spectroscopy (EIS) was obtained with AC amplitude of 5 mV (frequency: 0.1 Hz to 100 kHz). Mott Schottky (M–S) plots were measured in the potential range of +1.2 to +1.8 V (vs. Ag/AgCl), using a potential step at 200 Hz frequency.

3. Results and discussion

3.1. Characterization of samples

XRD. In Fig. 1, XRD pattern is shown to determine the effect of solvothermal reduction duration on the crystalline changes of the samples. Bare graphite powder showed a (002) peak at the diffraction angle of 26.6°, together with a smaller (101) peak at 54.7°. This result confirmed the structure of graphite.[30] After oxidizing, the (002) peak of pure GO (G-0) was shifted to 11.0°, and a (100) peak appeared at $2\theta = 42.6°$. This is due to the
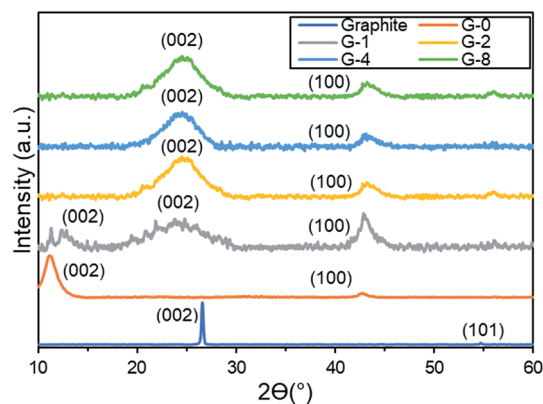

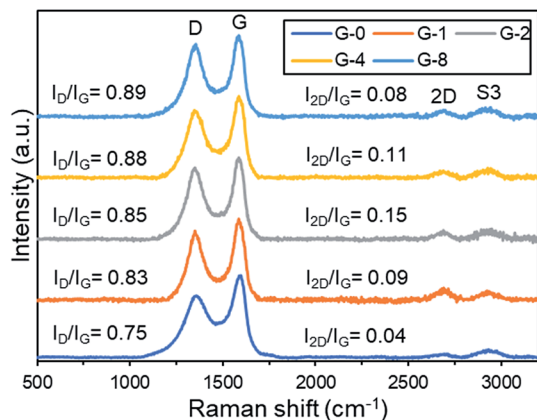Fig. 1 XRD patterns of bare graphite powder and G-0 to G-8.

Fig. 2 Raman analysis of G-0 to G-8.

intercalation of oxygenated functional groups (OFGs) into the graphitic layers.[31] After 1 h of reduction, G-1 had a broad peak that appeared at 24.8°, which indicated the occurrence of GO reduction.[32] However, a dispersed peak at 11.3° was also seen in G-1, this suggested that G-1 was only mildly reduced.[32] After 2 h of reduction, G-2 only showed a single (002) peak at 24.9°, suggesting that G-2 was successfully reduced to rGO.[33] As the reduction time was extended to 4 and 8 h, the (002) peak of G-4 and G-8 remained at the same position of 24.9°, this indicated the preservation of the rGO crystalline phase after >2 h of reduction.
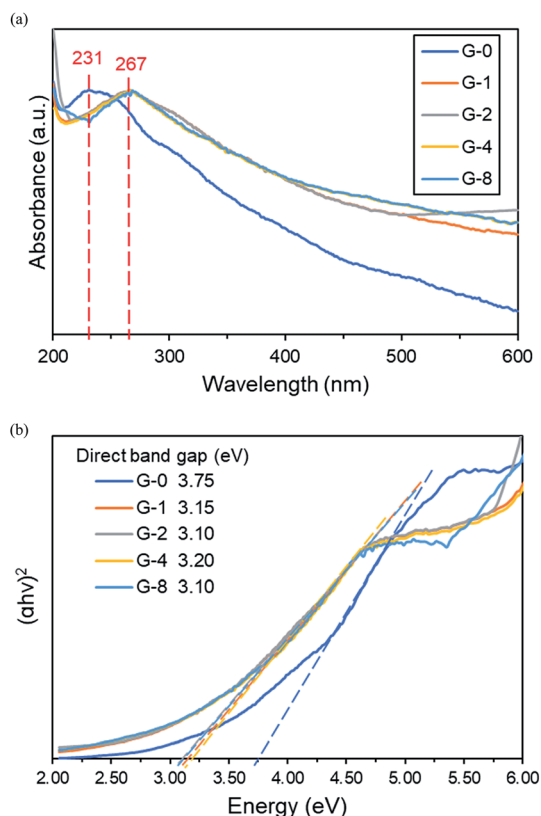

Fig. 3 (a) UV-Vis absorbance patterns of G-0 to G-8. (b) Tauc plot for direct band gap of G-0 to G-8.
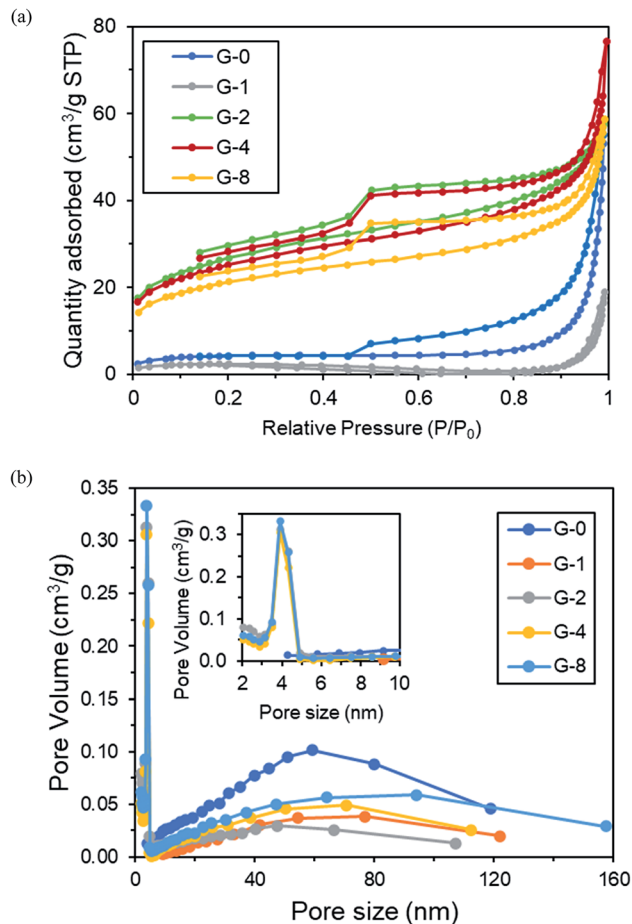

Fig. 4 (a) N_2 adsorption–desorption isotherms and (b) pore size plots of G-0 to G-8.

Raman. Fig. 2 shows the Raman spectra of the samples to examine the order of their graphitic structures. Four signature peaks of graphitic material were detected, namely D band ($\sim$1353 cm^{-1}) the structural disorderliness of graphene, G band ($\sim$1591 cm^{-1}) the scattering of the E_{2g} vibration mode of sp^2 C atoms, 2D band ($\sim$2693 cm^{-1}) the second-order of D band, and S3 band ($\sim$2936 cm^{-1}) the second-order of D–G peak combination.[34] The peak intensity ratio of D/G (I_D/I_G) represents the degree of disorder in the graphitic samples.[35] By increasing the reduction time, the I_D/I_G was increased from 0.75 (G-0) to 0.89 (G-8). The increment of I_D/I_G ratio indicated a greater degree of reduction.[36] Meanwhile, the peak intensity ratio of 2D/G (I_{2D}/I_G)

Table 1 BET/BJH textural parameters of G-0 to G-8

Sample	Surface area (m^2 g^{-1})	Pore size (nm)	Pore volume (cm^3 g^{-1})
G-0	15.03	59.42	0.085
G-1	8.20	76.86	0.029
G-2	94.81	3.89	0.118
G-4	89.13	3.89	0.101
G-8	75.20	3.90	0.090

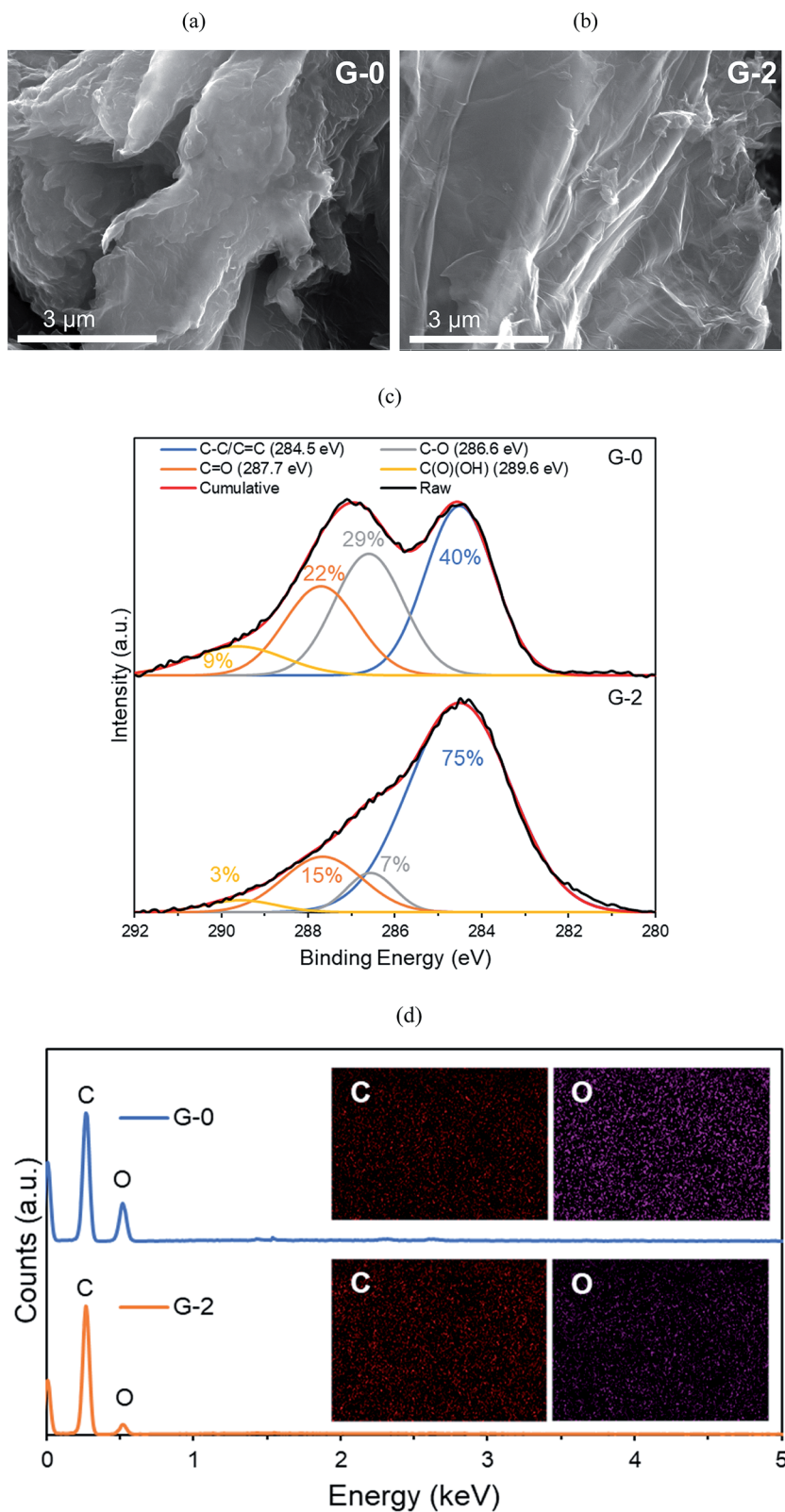(a)   (b)

(c)

(d)

Fig. 5   FESEM images of (a) G-0 and (b) G-2. (c) XPS C 1s and (d) EDX of G-0 and G-2.

can be used to estimate the relative amount of restored sp^2 fraction in rGO.[37] The I_{2D}/I_G ratio increased after reduction from 0.04 (G-0) to 0.15 (G-2), indicating the increment of sp^2 domain. However, the ratio then decreased upon longer reduction from 0.15 (G-2) to 0.08 (G-8). This suggested that prolonged reduction duration might have caused excessive graphitic defects, hence lesser sp^2 domains on the rGO surface.[38]
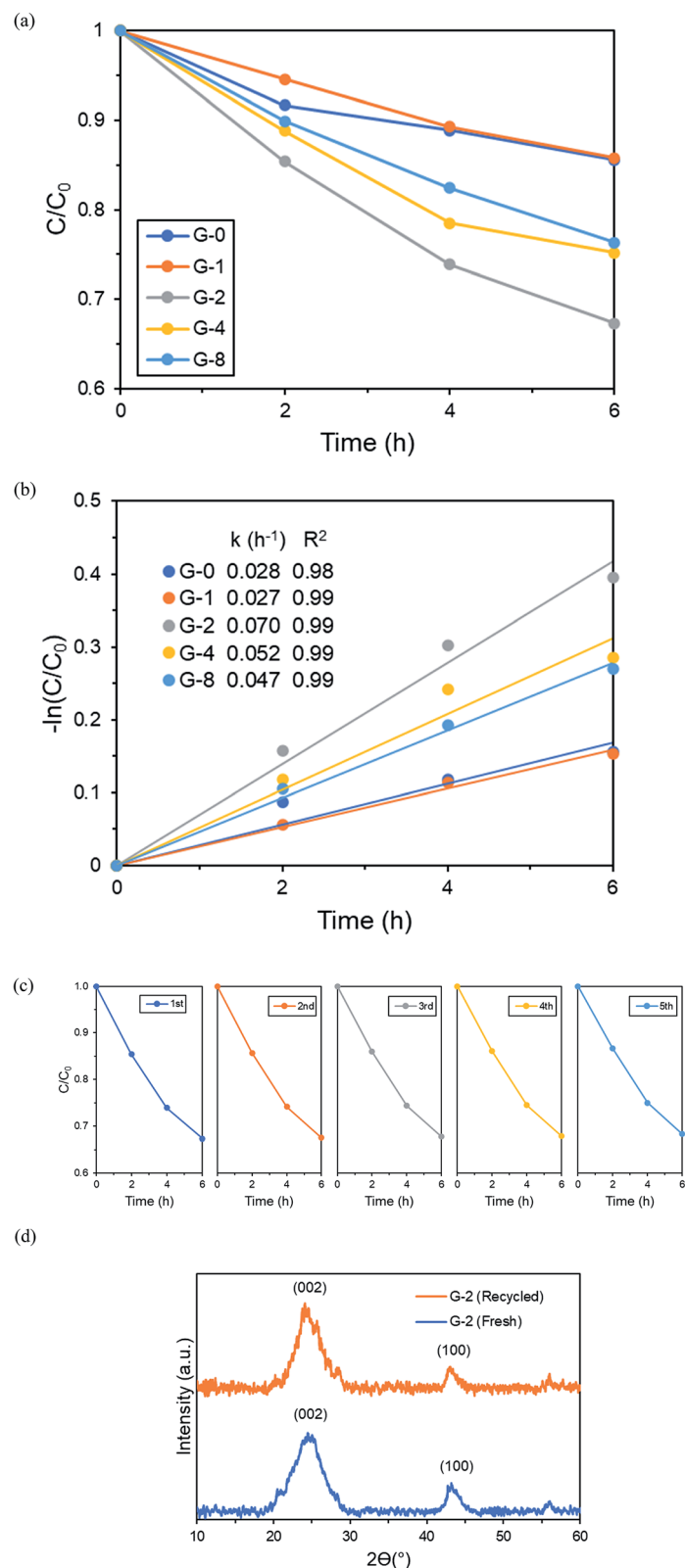
Fig. 6 Photodegradation of 50 ppm MB dye by G-0 to G-8 after 4 h of dark adsorptions. (b) Pseudo-first order kinetic plots. (c) Recycle test with G-2 for 6 h photodegradation of 50 ppm MB. (d) XRD of fresh and recycled G-2.

UV-Vis. Fig. 3a shows the UV-Vis absorption spectra of the samples. G-0 displayed a typical GO pattern with a 231 nm peak (π–π* transition of C=C) and a ~300 nm shoulder (n–π*

transition of C=O).[39] After solvothermal reduction, the 231 nm peak was red shifted to a higher wavelength of 267 nm, indicating the partial restoration of the conjugated sp^2 network.[40] Fig. 3b and
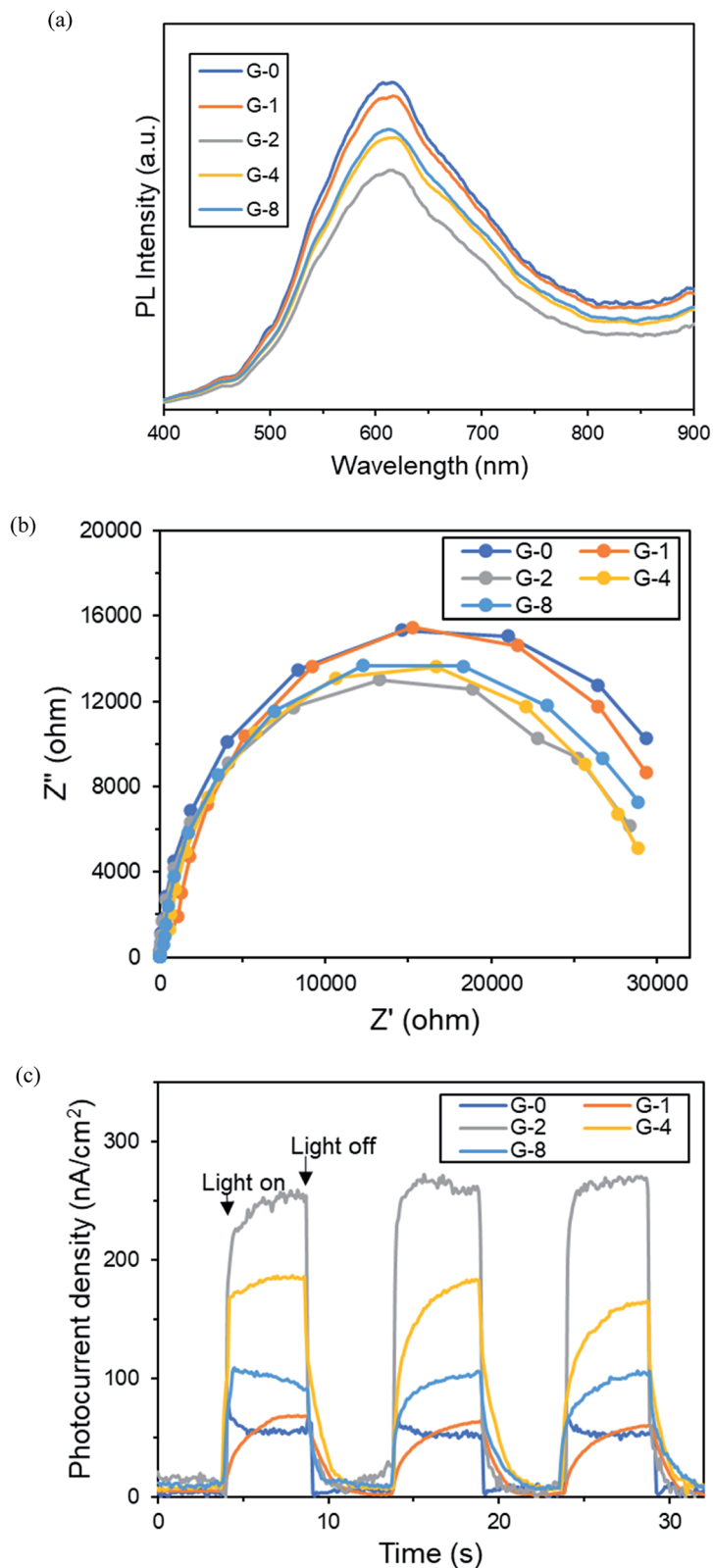
Fig. 7 (a) Photoluminescence (PL) patterns, (b) electrochemical impedance spectroscopy (EIS), and (c) transient photocurrent of G-0 to G-8.

S2† show the direct and indirect band gaps (E_{BG}) of G-0 to G-8, extrapolated by the linear fits of the Tauc plots. The direct band gap value was narrowed from 3.75 eV (G-0) to 3.10–3.20 eV (G-2 to G-8). The reduction of band gap was probably due to the partial removal of OFGs after solvothermal reduction. This is in concordance with previous studies, in which the quantity of OFGs is the main factor determining the band gap of a rGO.[41,42]

Specific surface area (SSA) and pore size distribution. Fig. 4a and Table 1 show the N_2 adsorption–desorption isotherms of G-0 to G-8. Based on the latest IUPAC classification,[43] the N_2 adsorption–desorption isotherms of all samples were type II with type H3 hysteresis loops. At $P/P_0 < 0.1$, the adsorption of N_2 increased gradually for all samples, this indicated the filling of micropores. For G-2, G-4, and G-8, the amount of N_2 adsorbed increased with increasing P/P_0 (0.1–0.8), indicating the conversion of monolayer to multilayer adsorption. Moreover, the hysteresis loops of G-2, G-4, and G-8 stopped at $P/P_0 \approx 0.45$, suggesting the existence of higher amount of micropores.[44] The adsorption of N_2 greatly increased at $P/P_0 > 0.9$ for all samples, owing to the presence of macropores.

From Fig. 4b and Table 1, the SSA of G-0 was 15.03 m^2 g^{-1}, pore size was 59.42 nm, and pore volume was 0.085 cm^3 g^{-1}. After solvothermal reduction of 2 h in G-2, the SSA was increased, pore size was reduced, and pore volume was increased. This could be due to the removal of OFGs, hence causing the changes on the G-2 surface morphology.[45] However, both G-4 and G-8 have lower SSA and pore volume than G-2, this was probably due to the agglomeration of the G-4 and G-8 rGO sheets after longer period of reduction.[46]

Morphology and surface bonding. The morphologies of G-0 and G-2 were investigated by FESEM. Fig. 5a shows that G-0 contained stacked sheets with flat surface. In contrast, sample G-2 had a sheet-like structure with wrinkled surface (Fig. 5b). The changes of surface morphology were possibly due to the removal of OFGs after solvothermal reduction.

To confirm that OFGs were removed from the GO sheets, XPS and EDX were conducted. In Fig. 5c, XPS C 1s results demonstrate that from G-0 to G-2, the C–O (epoxide and hydroxyl), C=O (carboxyl), and C(O)(OH) (carboxylic) groups were all partially reduced. In additional, EDX elemental mapping (Fig. 5d) shows that the O/C ratio was reduced from 0.56 (G-0) to 0.25 (G-2). Therefore, it is confirmed that OFGs were reduced by solvothermal reduction.

3.2. Photodegradation of MB dye

The dark adsorption–desorption equilibrium was reached after 4 h for all samples as shown in Fig. S3.† G-2 had the highest adsorption removal% at 29.3%, attributed to its highest SSA and pore volume. Meanwhile, only a small amount of MB was photodegraded by photolysis. All MB photodegradation tests were carried out after 4 h of dark adsorption. As shown in Fig. 6a and S4,† the efficiency of 6 h MB dye photodegradation was found to follow the order of G-2 > G-4 > G-8 > G-0 > G-1. From Fig. 6b, the pseudo-first order rate constant of G-2 (0.070 h^{-1}) was remarkably 2.5 times higher than the pristine GO sample G-0 (0.028 h^{-1}). Five cycles of 50 ppm MB dye photodegradation experiment were conducted by recycling the same G-2 photocatalyst, and no significant drop of photoactivity was noticed (Fig. 6c). Furthermore, Fig. 6d shows that the XRD of the recycled G-2 photocatalyst exhibited the same peaks as fresh G-2. This suggested that G-2 was still stable after consecutive photodegradation reactions.

3.3. Photoelectrochemical (PEC) measurements and photodegradation mechanism

PL, EIS, photocurrent. To confirm that the improvement of MB removal rate of G-2 during light reaction was due to enhanced photodegradation performance, a series of PEC measurements were conducted. The recombination rate of the photoinduced charge carriers is compared by photoluminescence (PL) emission spectra.[40] In Fig. 7a, all samples exhibited a broad peak between 400–800 nm. The G-2 sample had the lowest PL peak intensity, hence suggesting that G-2 had the lowest rate of recombination.

Next, the electrochemical impedance spectroscopy (EIS) of the samples were contrasted with Nyquist plot (Fig. 7b). In the Nyquist plot, the arc radius of the semi-circle implies the resistance of charge transportation of the photo-induced charges.[47] It was observed that G-2 had the smallest arc radius, hence the lowest charge transfer resistance. This was possibly due to the restoration of the conducting sp^2 fractions, as discussed in Raman analysis.

In Fig. 7c, transient photocurrent-time experiment with three on–off cycles of light illumination was performed to evaluate the photoinduced charge density of the samples. All samples displayed photocurrent values instantly upon light illumination, then the photocurrent diminished immediately with light off. The photocurrent density of G-2 was around five-fold of the original G-0. Moreover, the photocurrent densities were stable after 3 cycles, indicating good stability. By combining the results of PL, EIS, and photocurrent, it was determined that G-2 had enhanced ability to produce and separate photogenerated charges. Therefore G-2 exhibited a better performance in MB dye photodegradation rate than the other samples.

M–S. Fig. 8 shows the Mott–Schottky (M–S) plot of G-0 and G-2. Both samples exhibited negative slopes, suggesting that they were p-type semiconductors.[48] The flatband potential value (E_{FB}) can be determined from the x-axis interception of the linear line of the M–S curve.[49] The E_{FB} (vs. Ag/AgCl, pH 6.5) of G-0 and G-2 were +1.75 V and +1.69 V, respectively. Generally, the valence band potential (E_{VB}) of a p-type semiconductor is approximately +0.3 V from the corresponding flat band potential,[50] thus the
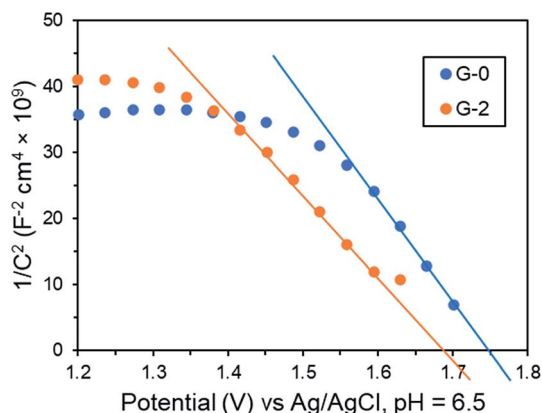

Fig. 8 Mott–Schottky plot of G-0 and G-2.

E_{VB} of G-0 and G-2 were +2.05 V and +1.99 V (*vs.* Ag/AgCl, pH 6.5). After converting the E_{VB} *versus* Ag/AgCl, pH 6.5 to *versus* normal hydrogen electrode (NHE), pH 7 (eqn (S1)†), the E_{VB} of G-0 was +2.23 V and G-2 was +2.17 V. In addition, the acceptor (hole) mobile carrier concentrations of the p-type G-0 and G-2 can be quantified as shown in eqn (S2).† The acceptor charge density of G-0 was 9.28×10^{15} cm^{-3} and for G-2 was 1.16×10^{16} cm^{-3}. The enhancement of charge density is in agreement with a past study, in which a rGO with greater reduction degree has a higher charge density than another rGO with lesser reduction.[51] This is because rGO with a greater reduction degree has a higher concentration of π electron, hence resulting in an increase of charge density.[52] The higher charge density of G-2 could have been beneficial to the efficiency of MB dye photodegradation.
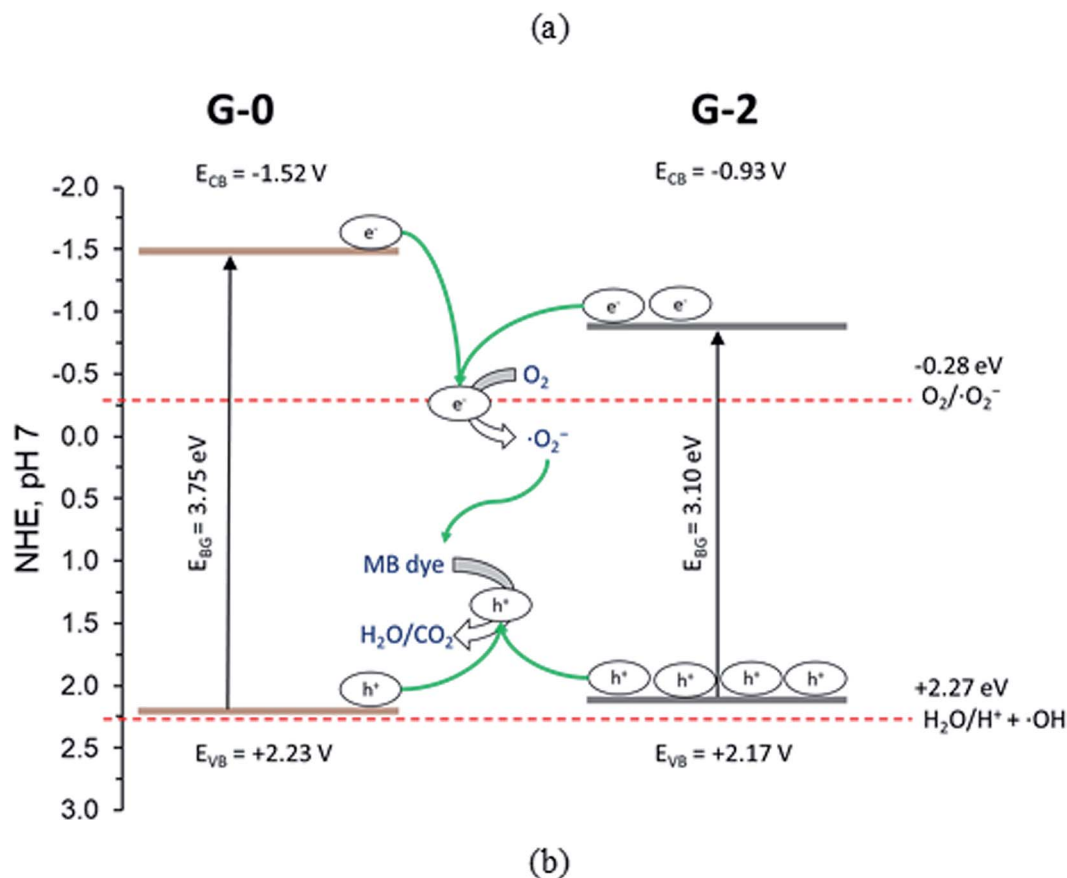

Fig. 9 (a) Proposed mechanism for MB photodegradation by G-0 and G-2. (b) Photoactivity of G-2 in the presence of different scavenging agents.

3.4. Mechanism

The conduction band potential (E_{CB}) of G-0 and G-2 were computed to be -1.52 V and -0.93 V (vs. NHE, pH 7) by eqn (S3).† Therefore, the electronic band structures of G-0 and G-2 can be illustrated as Fig. 9. From G-0 to G-2, the band gap was reduced from 3.75 eV to 3.10 eV, the E_{VB} was shifted negatively for 0.06 V, and the E_{CB} was shifted positively for 0.59 V. Similar observation was also observed in a previous study, in which the E_{VB} and E_{CB} of GO were shifted after partial reduction.[53] The shifting of band locations is due to the changes of the relative ratios of OFGs.[54] The E_{CB} of G-0 and G-2 were negative enough to carry out the reduction O_2 to $^\cdot O_2^-$ radical (-0.28 V vs. NHE, pH 7 (ref. 55)), however their E_{VB} were not positive enough to oxidize H_2O to H^+ and $^\cdot OH$ radical (+2.27 V vs. NHE, pH 7 (ref. 55)). Hence, it was proposed that the main mechanism for G-0 and G-2 to photodegrade MB dye were through the photogenerated h^+ and $^\cdot O_2^-$ radical.

To verify the proposed mechanism, three reactive species trapping tests were conducted on G-2 photodegradation of MB dye. In the trapping tests, $^\cdot O_2^-$ radical was removed by bubbling pure nitrogen (N_2) gas into the MB dye solution, h^+ species was scavenged by 10 mM of ammonium oxalate (AO), and $^\cdot OH$ radical was trapped by 10 mM of isopropyl alcohol (IPA). Based on Fig. 9b, 33% of dye was removed via photodegradation when no scavenger was added. In the presence of N_2 and AO, the photodegradation performance dropped to 24% and 20% respectively. In contrast, the presence of IPA did not significantly affect the photodegradation activity. Thus, the results confirmed that h^+ and $^\cdot O_2^-$ radical were the major reactive species in the photoactivity of G-2.

Conclusion

The 2 h solvothermally reduced rGO sample (G-2) had an improved performance to photodegrade MB dye in contrast to pristine GO (G-0). Through systematic characterizations and PEC measurements, it was confirmed that the improved MB dye removal rate of G-2 was due to enhanced photoactivity. The enhanced photoactivity of G-2 was mainly attributed to its higher charge carrier density, better ability to separate charge carriers, and higher photocurrent density. By using radical scavenger tests and constructing the electronic band structures of G-0 and G-2, it was determined that the photogenerated h^+ and $^\cdot O_2^-$ radical played major roles in GO/rGO MB dye photodegradation.

Conflicts of interest

There are no conflicts to declare.

Acknowledgements

References

1 V. L. E. Siong, et al., One-step Solvothermal Synthesis of rGO/TiO$_2$ Nanocomposite for Efficient Solar Photocatalytic Degradation of Methylene Blue Dye, Curr. Nanosci., 2019, 15(2), 157–162.

2 Z. Carmen and S. Daniela, Textile organic dyes–characteristics, polluting effects and separation/elimination procedures from industrial effluents–a critical overview, in Organic pollutants ten years after the Stockholm convention-environmental and analytical update, InTech Rijeka, Croatia, 2012.

3 Y. R. Smith, A. Kar and V. Subramanian, Investigation of physicochemical parameters that influence photocatalytic degradation of methyl orange over TiO$_2$ nanotubes, Ind. Eng. Chem. Res., 2009, 48(23), 10268–10276.

4 K. M. Lee, et al., Recent developments of zinc oxide based photocatalyst in water treatment technology: a review, Water Res., 2016, 88, 428–448.

5 X. Liu, et al., Integrating the Z-scheme heterojunction into a novel Ag$_2$O@rGO@reduced TiO$_2$ photocatalyst: Broadened light absorption and accelerated charge separation co-mediated highly efficient UV/visible/NIR light photocatalysis, J. Colloid Interface Sci., 2019, 538, 689–698.

6 Z. Liang, et al., Full solar spectrum photocatalytic oxygen evolution by carbon-coated TiO$_2$ hierarchical nanotubes, Appl. Catal., B, 2019, 243, 711–720.

7 Y. Xue, et al., Porous graphitic carbon nitride with nitrogen defects and cobalt–nitrogen (CoN) bonds for efficient broad spectrum (visible and near-infrared) photocatalytic H$_2$ production, J. Colloid Interface Sci., 2020, 561, 719–729.

8 Y. Guo, et al., Non-high temperature method to synthesize carbon coated TiO$_2$ nano-dendrites for enhanced wide spectrum photocatalytic hydrogen evolution activity, J. Colloid Interface Sci., 2020, 412–418.

9 K. Krishnamoorthy, R. Mohan and S.-J. Kim, Graphene oxide as a photocatalytic material, Appl. Phys. Lett., 2011, 98(24), 244101.

10 Z. Xiong, et al., Photocatalytic degradation of dyes over graphene–gold nanocomposites under visible light irradiation, Chem. Commun., 2010, 46(33), 6099–6101.

11 Z. Xiong, L. L. Zhang and X. S. Zhao, Visible-Light-Induced Dye Degradation over Copper-Modified Reduced Graphene Oxide, Chem.–Eur. J., 2011, 17(8), 2428–2434.

12 Y. Zhao, et al., Enhanced photocatalytic properties of ZnO/reduced graphene oxide sheets (rGO) composites with controllable morphology and composition, Appl. Surf. Sci., 2017, 412, 58–68.

13 K. Govindan, et al., Effect of peroxomonosulfate, peroxodisulfate and hydrogen peroxide on graphene oxide photocatalytic performances in methyl orange dye degradation, Chemosphere, 2019, 237, 124479.

14 F. Wang, Preparation of N-Doped Graphene and Its Performance in Degradation of Methyl Orange, Russ. J. Phys. Chem. A, 2019, 93(11), 2263–2268.

15 R. Raliya, *et al.*, Photocatalytic degradation of methyl orange dye by pristine titanium dioxide, zinc oxide, and graphene oxide nanostructures and their composites under visible light irradiation, *Appl. Nanosci.*, 2017, **7**(5), 253–259.

16 J. Liu, *et al.*, Enhanced photocatalytic performance of partially reduced graphene oxide under simulated solar light through loading gold nanoparticles, *Mater. Lett.*, 2014, **134**, 134–137.

17 M. Singh, *et al.*, Boron doped graphene oxide with enhanced photocatalytic activity for organic pollutants, *J. Photochem. Photobiol., A*, 2018, **364**, 130–139.

18 B. Su, *et al.*, Enhanced photocatalytic performance of ZnO/rGO composite materials prepared *via* an improved two-steps method, *Ceram. Int.*, 2016, **42**(6), 7632–7638.

19 S. Kumar and A. Kumar, Chemically derived luminescent graphene oxide nanosheets and its sunlight driven photocatalytic activity against methylene blue dye, *Opt. Mater.*, 2016, **62**, 320–327.

20 M. Singh, *et al.*, Study of photocatalytic and antibacterial activities of graphene oxide nanosheets, *Adv. Compos. Hybrid Mater.*, 2018, **1**(4), 759–765.

21 C. P. P. Wong, *et al.*, Advanced chemical reduction of reduced graphene oxide and its photocatalytic activity in degrading reactive black 5, *Materials*, 2015, **8**(10), 7118–7128.

22 V. L. E. Siong, *et al.*, Removal of methylene blue dye by solvothermally reduced graphene oxide: a metal-free adsorption and photodegradation method, *RSC Adv.*, 2019, **9**(64), 37686–37695.

23 L. Guardia, *et al.*, UV light exposure of aqueous graphene oxide suspensions to promote their direct reduction, formation of graphene–metal nanoparticle hybrids and dye degradation, *Carbon*, 2012, **50**(3), 1014–1024.

24 H. Moussa, *et al.*, ZnO rods/reduced graphene oxide composites prepared *via* a solvothermal reaction for efficient sunlight-driven photocatalysis, *Appl. Catal., B*, 2016, **185**, 11–21.

25 B. Xue and Y. Zou, High photocatalytic activity of ZnO–graphene composite, *J. Colloid Interface Sci.*, 2018, **529**, 306–313.

26 Y. Zheng, *et al.*, Mg 0.8 Zn 0.2 O microspheres: preparation, characterization and application for degrading organic dyes, *CrystEngComm*, 2020, **22**(7), 1273–1285.

27 L. Tian, S. Min and F. Wang, Integrating noble-metal-free metallic vanadium carbide cocatalyst with CdS for efficient visible-light-driven photocatalytic H_2 evolution, *Appl. Catal., B*, 2019, **259**, 118029.

28 A. Kumar, S. Samanta and R. Srivastava, Systematic investigation for the photocatalytic applications of carbon nitride/porous zeolite heterojunction, *ACS Omega*, 2018, **3**(12), 17261–17275.

29 Q. Li, *et al.*, Z-scheme BiOCl-Au-CdS heterostructure with enhanced sunlight-driven photocatalytic activity in degrading water dyes and antibiotics, *ACS Sustainable Chem. Eng.*, 2017, **5**(8), 6958–6968.

30 M. Fathy, *et al.*, Optimizing the preparation parameters of GO and rGO for large-scale production, *J. Mater. Sci.*, 2016, **51**(12), 5664–5675.

31 V. Loryuenyong, *et al.*, Preparation and characterization of reduced graphene oxide sheets *via* water-based exfoliation and reduction methods, *Adv. Mater. Sci. Eng.*, 2013, **2013**, 923403.

32 H.-H. Huang, *et al.*, Structural evolution of hydrothermally derived reduced graphene oxide, *Sci. Rep.*, 2018, **8**(1), 1–9.

33 D. Hou, *et al.*, Facile synthesis of graphene *via* reduction of graphene oxide by artemisinin in ethanol, *J. Materiomics*, 2018, **4**(3), 256–265.

34 K. Krishnamoorthy, *et al.*, The chemical and structural analysis of graphene oxide with different degrees of oxidation, *Carbon*, 2013, **53**, 38–49.

35 K. Spilarewicz-Stanek, *et al.*, Elucidation of the function of oxygen moieties on graphene oxide and reduced graphene oxide in the nucleation and growth of silver nanoparticles, *RSC Adv.*, 2016, **6**(65), 60056–60067.

36 X. Mei, X. Meng and F. Wu, Hydrothermal method for the production of reduced graphene oxide, *Phys. E*, 2015, **68**, 81–86.

37 S. Mortazavi, *et al.*, Modification of graphene oxide film properties using KrF laser irradiation, *RSC Adv.*, 2018, **8**(23), 12808–12814.

38 V. Labunov, *et al.*, Features of the reduction of graphene from graphene oxide, *Russ. J. Phys. Chem. A*, 2017, **91**(6), 1088–1092.

39 S. Xu, L. Yong and P. Wu, One-pot, green, rapid synthesis of flowerlike gold nanoparticles/reduced graphene oxide composite with regenerated silk fibroin as efficient oxygen reduction electrocatalysts, *ACS Appl. Mater. Interfaces*, 2013, **5**(3), 654–662.

40 X. H. Tai, *et al.*, Effective photoreduction of graphene oxide for photodegradation of volatile organic compounds, *RSC Adv.*, 2019, **9**(31), 18076–18086.

41 Y. Jin, *et al.*, Band gap of reduced graphene oxide tuned by controlling functional groups, *J. Mater. Chem. C*, 2020, **8**(14), 4885–4894.

42 A. H. de Lima, *et al.*, Origin of optical bandgap fluctuations in graphene oxide, *Eur. Phys. J. B*, 2020, **93**(6), 1–12.

43 M. Thommes, *et al.*, Physisorption of gases, with special reference to the evaluation of surface area and pore size distribution (IUPAC Technical Report), *Pure Appl. Chem.*, 2015, **87**(9–10), 1051–1069.

44 H. Moussa, *et al.*, ZnO rods/reduced graphene oxide composites prepared *via* a solvothermal reaction for efficient sunlight-driven photocatalysis, *Appl. Catal., B*, 2016, **185**, 11–21.

45 B. Zhao, *et al.*, Supercapacitor performances of thermally reduced graphene oxide, *J. Power Sources*, 2012, **198**, 423–427.

46 B. D. Ossonon and D. Bélanger, Synthesis and characterization of sulfophenyl-functionalized reduced graphene oxide sheets, *RSC Adv.*, 2017, **7**(44), 27224–27234.

47 L. K. Putri, *et al.*, Insights on the impact of doping levels in oxygen-doped g-C$_3$N$_4$ and its effects on photocatalytic activity, *Appl. Surf. Sci.*, 2020, **504**, 144427.

48 A. Samal, D. P. Das and G. Madras, Repercussion of Solid state *vs.* Liquid state synthesized pn heterojunction RGO-copper phosphate on proton reduction potential in water, *Sci. Rep.*, 2018, **8**(1), 1–18.

49 P. Wang, *et al.*, The fundamental role and mechanism of reduced graphene oxide in rGO/Pt-TiO$_2$ nanocomposite for high-performance photocatalytic water splitting, *Appl. Catal., B*, 2017, **207**, 335–346.

50 W. Yin, *et al.*, Embedding metal in the interface of a pn heterojunction with a stack design for superior Z-scheme photocatalytic hydrogen evolution, *ACS Appl. Mater. Interfaces*, 2016, **8**(35), 23133–23142.

51 N. D. K. Tu, *et al.*, Remarkable conversion between n-and p-type reduced graphene oxide on varying the thermal annealing temperature, *Chem. Mater.*, 2015, **27**(21), 7362–7369.

52 T. Sreeprasad and V. Berry, How do the electrical properties of graphene change with its functionalization?, *Small*, 2013, **9**(3), 341–350.

53 X. Xu, *et al.*, An Efficient p–n Heterojunction Photocatalyst Constructed from a Coordination Polymer Nanoplate and a Partially Reduced Graphene Oxide for Visible-Light Hydrogen Production, *Chem.–Eur. J.*, 2015, **21**(41), 14638–14647.

54 L. Guo, *et al.*, Bandgap tailoring and synchronous microdevices patterning of graphene oxides, *J. Phys. Chem. C*, 2012, **116**(5), 3594–3599.

55 L. Wu, C. Y. Jimmy and X. Fu, Characterization and photocatalytic mechanism of nanosized CdS coupled TiO$_2$ nanocrystals under visible light irradiation, *J. Mol. Catal. A: Chem.*, 2006, **244**(1–2), 25–32.